Theoretical and Experimental Study of Weakly Bound CO2-(pH(2))(2) Trimers

4 AUTHORS, INCLUDING:

Hui Li
Jilin University
43 PUBLICATIONS   371 CITATIONS

SEE PROFILE

Robert Le Roy
University of Waterloo
197 PUBLICATIONS   5,003 CITATIONS

SEE PROFILE

Pierre-Nicholas Roy
University of Waterloo
102 PUBLICATIONS   1,350 CITATIONS

SEE PROFILE

ARTICLE

Theoretical and Experimental Study of Weakly Bound $CO_2-(pH_2)_2$ Trimers

Hui Li,[†,‡] A. R. W. McKellar,[§] Robert J. Le Roy,[†] and Pierre-Nicholas Roy[*,†]

[†]Department of Chemistry, University of Waterloo, Waterloo, Ontario N2L 3G1, Canada

[‡]Institute of Theoretical Chemistry, State Key Laboratory of Theoretical and Computational Chemistry, Jilin University, 2519 Jiefang Road, Changchun 130023, People's Republic of China

[§]Steacie Institute for Molecular Sciences, National Research Council of Canada, Ottawa, Ontario K1A OR6, Canada

Ⓢ *Supporting Information*

ABSTRACT: The infrared spectrum of $CO_2-(pH_2)_2$ trimers is predicted by performing exact basis-set calculations on a global potential energy surface defined as the sum of accurately known two-body pH_2-CO_2 (*J. Chem. Phys.* 2010, *132*, 214309) and pH_2-pH_2 potentials (*J. Chem. Phys.* 2008, *129*, 094304). These results are compared with new spectroscopic measurements for this species, for which 13 transitions are now assigned. A reduced-dimension treatment of the pH_2 rotation has been employed by applying the hindered-rotor averaging technique of Li, Roy, and Le Roy (*J. Chem. Phys.* 2010, *133*, 104305). Three-body effects and the quality of the potential are discussed. A new technique for displaying the three-dimensional pH_2 density in the body-fixed frame is used, and shows that in the ground state the two pH_2 molecules are localized much more closely together than is the case for the two He atoms in the analogous $CO_2-(He)_2$ species. A clear tunneling splitting is evident for the torsional motion of the two pH_2 molecules on a ring about the CO_2 molecular axis, in contrast to the case of $CO_2-(He)_2$ where a more regular progression of vibrational levels reflects the much lower torsional barrier.
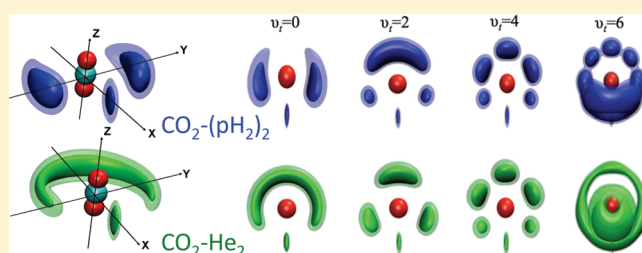
I. INTRODUCTION

Since the pioneering prediction of superfluidity in pure para-hydrogen clusters by Sindzingre, Ceperley, and Klein,[1] several theoretical studies have focused on the properties of low temperature hydrogen clusters.[2−15] In recent years, spectroscopic studies of molecules embedded in helium clusters and droplets and in para-hydrogen (pH_2) clusters have provided a unique opportunity to study quantum solvation and microscopic superfluidity.[16−27] Such studies provide a new route for investigating the superfluid properties of pH_2 by considering pH_2 clusters doped with a single chromophore molecule.[28−39] In a study based on use of the CO_2 molecule as a probe, we recently reported the first experimental determination of the molecular superfluid fraction of para-hydrogen.[39] It was found that the experimental behavior of the superfluid fraction as a function of cluster size was consistent with theoretical predictions based on path integral Monte Carlo simulations.

To fully understand the experimental spectra on the atomic scale requires complementary computer simulation studies using accurate intermolecular potential energy functions,[40,41] and a number of quantum Monte Carlo simulations of He clusters containing dopants such as OCS, N_2O, CO_2, CO, and HCCCN have been reported which yielded excellent agreement with experiment.[41−52] Studies of dimer and trimer complexes are an essential starting point for testing two-body potential energy

surfaces, for looking for three-body effects, and for testing the validity of quantum Monte Carlo methods for molecular clusters, since comparisons with exact quantum results are possible.

Exact quantum calculation of infrared and microwave spectra for trimer species containing one OCS, N_2O, CO_2, or CO molecule attached to two He atoms have been reported by Wang and Carrington and co-workers[53−56] and by Li et al.[57] To date, however, such calculations involving pH_2 adducts have been limited to dimers formed with a single attached pH_2 molecule.[49,58−62] For the particular case of the CO_2-H_2 complex, experimental results are available in the form of infrared spectra.[58,63] In the present paper, we extend such exact quantum calculations to the case of two pH_2 molecules attached to one CO_2 dopant molecule. The results are used to help assign the experimental infrared spectrum of $CO_2-(pH_2)_2$, and good agreement is obtained. We find that the low frequency vibrational dynamics of $CO_2-(pH_2)_2$ are dominated by a "torsional" motion in which the two pH_2 molecules move relative to one another on a ring around the CO_2 molecular axis, similar to the
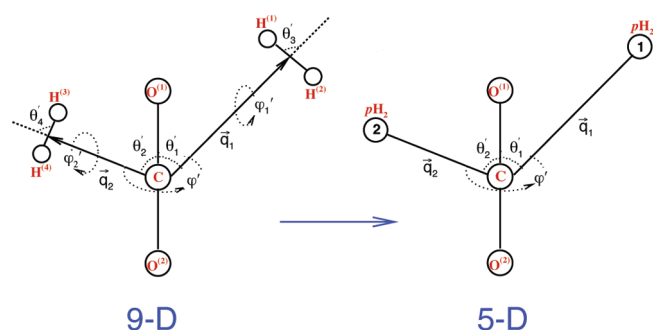
Figure 1. Jacobi coordinates for the $CO_2-(H_2)_2$ complex: left side, the geometry described with nine dimensions of intermolecular coordinates; right side, the geometry described with five dimensions of intermolecular coordinates and with the two para-hydrogen treated as spherical particles.

situation for trimers containing two He atoms. However, there is a big difference. In the helium case, the lowest torsional levels lie very near the maximum of the barrier to free torsional motion, resulting in a relatively large tunneling splitting (≈ 0.5 cm^{-1}), whereas in the hydrogen case explored here, the lowest torsional levels lie well below the top of that barrier so the splitting is much smaller (≈ 0.1 cm^{-1}), despite hydrogen's lighter mass.

II. THEORY AND METHODS

A. Geometry and Reduced-Dimension Treatment. The $CO_2-(pH_2)_2$ system contains seven atoms, and hence may be described in terms of 15-dimensional (15D) ($3 \times 7 - 6 = 15$) coordinates. If we consider only the intermolecular coordinates, treating linear CO_2 and the two H_2 as rigid molecules, there are still nine remaining intermolecular degrees of freedom. The geometry of this complex can be described naturally using the nine Jacobi coordinates ($q_1, q_2, \theta'_1, \theta'_2, \theta'_3, \theta'_4, \varphi', \varphi'_1, \varphi'_2$) defined as shown on the left panel of Figure 1. Here, q_1 and q_2 are the distances from the center of mass of CO_2 to the centers of mass of the two H_2 molecules, θ'_1 and θ'_2 are the angles between $\vec{q}_1$ or $\vec{q}_2$ and a vector pointing from atom $O^{(2)}$ to atom $O^{(1)}$, θ'_3 and θ'_4 are the angles between $\vec{q}_1$ and a vector pointing from atom $H^{(2)}$ to atom $H^{(1)}$, and from $\vec{q}_2$ to a vector pointing from atom $H^{(4)}$ to atom $H^{(3)}$, φ' is the dihedral angle between two planes defined by vector $\vec{q}_1$ and $\vec{q}_2$ with the axis of the CO_2 molecule, and φ'_1 and φ'_2 are the dihedral angles for rotation of $H^{(1)}-H^{(2)}$ and $H^{(3)}-H^{(4)}$ about vectors $\vec{q}_1$ or $\vec{q}_2$, respectively, relative to the alignment of the CO_2 molecule.

Exact quantum solution of the resulting nine-dimensional (9D) intermolecular Schödinger equation for the $CO_2-(pH_2)_2$ trimer is still hard to do. However, we know that an isolated ground-state ($J = 0$) H_2 molecule is precisely spherically symmetric, and because the energy spacing to its first excited ($J = 2$) level is relatively large, it is often considered a good approximation to treat pH_2 as a spherical particle. If we treat the two pH_2 molecules in a $CO_2-(pH_2)_2$ complex as spherical particles, the 9D intermolecular coordinates for a $CO_2-(pH_2)_2$ complex would be reduced to the five coordinates ($q_1, q_2, \theta'_1, \theta'_2, \varphi'$) shown on the right-hand side of Figure 1. This is an attractive approximation, and its use would greatly reduce the computational effort. However, pH_2 is not truly spherically symmetric in H_2-molecule interactions, and performing a simple spherical average over the relative

orientations of the H_2 moiety does not provide an accurate description.[64]

Recently, Li, Roy, and Le Roy introduced an "adiabatic-hindered-rotor" approximation method to reduce the dimensionality associated with pH_2 in (pH_2)–molecule and larger clusters. Comparisons were made for pH_2 with CO_2, with CO, and with itself, and the results showed that use of an "adiabatic-hindered-rotor" separation of the fast rotational motion of pH_2 from the other degrees of freedom yields *effective* spherical descriptions of pH_2 in pH_2-{linear molecule} interactions that are an order of magnitude more accurate than those obtained using a simple-spherical-average approximation.[64] Therefore, a relatively good reduced-dimension treatment of $CO_2-(pH_2)_2$ trimers should be obtained by applying the "adiabatic-hindered rotor approximation" which allows the system to be described accurately in terms of the reduced-dimension 5D coordinates ($q_1, q_2, \theta'_1, \theta'_2, \varphi'$) shown on the right side of Figure 1.

B. Hamiltonian. The methodology used in this work is based mainly on the work of Wang and Carrington[53] and on fundamental ideas presented by Mladenovic.[65] Wang and Carrington applied their approach to the $N_2O-(He)_2$ system and were able to reproduce experimentally observable rovibrational transitions quite accurately. They also used their approach to treat $CO_2-(He)_2$ and $CO-(He)_2$ complexes, again with great success.[54,55] The method is briefly reviewed here, and the reader is referred to ref 53 for further details.

The rovibrational Hamiltonian of the $CO_2-(pH_2)_2$ complex in the body-fixed frame has the following form (in a.u.)[53,65–67]

$$\hat{H} = \hat{T}_{str} + \hat{T}_{diag} + \hat{T}_{off} + \hat{T}_{Cor} + \overline{V}(r_1, r_2, \theta_1, \theta_2, \phi) \quad (1)$$

with

$$\hat{T}_{str} = -\frac{1}{2m_{H_2}}\frac{\partial^2}{\partial r_1^2} - \frac{1}{2m_{H_2}}\frac{\partial^2}{\partial r_2^2} \quad (2)$$

$$\hat{T}_{diag} = $$
$$-\left(\frac{1}{2m_{H_2}r_1^2} + B_{CO_2}\right)\left[\frac{\partial^2}{\partial\theta_1^2} + \cot\theta_1\frac{\partial}{\partial\theta_1} - \frac{1}{\sin^2\theta_1}(\hat{J}_z - \hat{l}_{2z})^2\right]$$
$$+ \left[\frac{1}{2m_{H_2}r_2^2} + B_{CO_2}\right]\hat{l}_2^2 + B_{CO_2}[\hat{J}^2 - 2(\hat{J}_z - \hat{l}_{2z})^2 - 2\hat{J}_z\hat{l}_{2z}] \quad (3)$$

$$\hat{T}_{off} = B_{CO_2}[\hat{l}_{2+}\hat{a}_1^- + \hat{l}_{2-}\hat{a}_1^+] \quad (4)$$

$$\hat{T}_{Cor} = -B_{CO_2}[\hat{J}_-\hat{a}_1^+ + \hat{J}_+\hat{a}_1^- + \hat{J}_-\hat{l}_{2+} + \hat{J}_+\hat{l}_{2-}] \quad (5)$$

in which

$$\hat{J}_\pm = \hat{J}_x \pm i\hat{J}_y, \quad \hat{l}_{2\pm} = \hat{l}_{2x} \pm i\hat{l}_{2y} \quad (6)$$

$$\hat{a}_1^\pm = \pm\frac{\partial}{\partial\theta_1} - \cot\theta_1(\hat{J}_z - \hat{l}_{2z}) \quad (7)$$

Details of the coordinate system are illustrated in Figure 2: r_1 and r_2 are the lengths of Radau (or orthogonalized satellite) vectors $\vec{r}_1$ and $\vec{r}_2$, which are linear combinations of the Jacobi (or satellite) vectors $\vec{q}_1$ and $\vec{q}_2$ running from the center of mass of CO_2 to the centers of the pH_2 molecules.[65] The polyspherical angles (θ_1, θ_2, ϕ) are determined by the three vectors ($\vec{r}_0, \vec{r}_1, \vec{r}_2$), where $\vec{r}_0$ is a vector along the axis of CO_2, m_{H_2} is the mass of the
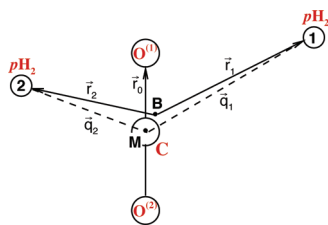
Figure 2. M is the center of mass of CO_2, and B is the canonical point for the Radau vectors. $\vec{q}_1$ and $\vec{q}_2$ are Jacobi vectors. $\vec{r}_1$ and $\vec{r}_2$ are Radau vectors. φ is a dihedral angle between $\vec{r}_1$ and $\vec{r}_2$ around $\vec{r}_0$. θ_1 (θ_2) are angles between $\vec{r}_0$ and $\vec{r}_1$ ($\vec{r}_2$).

pH_2 molecule, and B_{CO_2} is the inertial rotation constant of CO_2. The operators $\hat{J}_x$, $\hat{J}_y$, and $\hat{J}_z$ are the components of the total angular momentum operator $\hat{J}$ in the body-fixed frame, the z axis of the body-fixed frame lies along the Jacobi radial vector $\vec{r}_0$, and its x axis lies in the plane that contains the vector $\vec{r}_0$ and one pH_2 molecule. Here $\overline{V}(r_1, r_2, \theta_1, \theta_2, \phi)$ is the total potential energy function which is represented as a sum of two two-dimensional "adiabatic-hindered-rotor" pH_2−CO_2 potentials[60,64] plus the one-dimensional adiabatic-hindered-rotor pH_2−pH_2[68] intermolecular potential. The above Hamiltonian contains full vibration−rotation coupling.

C. Basis Function, Symmetry, and Matrix Elements. A sine discrete variable representation (DVR) grid[69,70] is used for the radial degree of freedom, while parity-adapted rovibrational basis functions are used for the angular part.[53] The latter are linear combinations of the functions

$$\langle \theta_1, \theta_2, \phi; \alpha, \beta, \gamma | l_1, l_2, m_2; J, K, M \rangle$$
$$= \sqrt{\frac{2J+1}{8\pi^2}} \Theta_{l_1}^{K-m_2}(\theta_1) Y_{l_2}^{m_2}(\theta_2, \phi) D_{M,K}^{J*}(\alpha, \beta, \gamma) \quad (8)$$

with

$$Y_{l_2}^{m_2}(\theta_2, \phi) = \frac{1}{\sqrt{2\pi}} \Theta_{l_2}^{m_2}(\theta_2) e^{im_2\phi} \quad (9)$$

where $\Theta_l^{m_2}$, $Y_l^{m_2}$, and $D_{M,K}^J$ are, respectively, the normalized associated Legendre function with the $(-1)^{m_2}$ Condon−Shortley phase factor,[71] spherical harmonic functions, and Wigner functions.[71] The body-fixed frame is related to the space-fixed frame via a rotation in the three Euler angles (α, β, γ). The projection of the total angular momentum J onto the space-fixed or body-fixed frame is given by M or K, respectively.

The molecular symmetry group of the CO_2−$(pH_2)_2$ trimer includes the inversion operation E^*, permutation of the two pH_2 molecules, denoted as (12), and permutation of two O nuclei, denoted as (34). Therefore, the CO_2−$(pH_2)_2$ system belongs to the permutation-inversion group $G_8 = \{E, E^*\} \otimes \{E, (12)\} \otimes \{E, (34)\}$. The irreducible representation labels are defined as follows: A and B label symmetry with respect to permutation of the pH_2, subscripts 1 and 2 label symmetry with respect to permutation of the O nuclei, and superscripts $+$ and $-$ are the parity labels. Because pH_2 and ^{16}O are both bosons with zero nuclear spin, the rovibrational wave functions are required to be symmetric under permutations of pH_2 and of ^{16}O. Therefore, only A_1^+ and A_1^- symmetry states are physically allowed. This removes roughly 75% of the otherwise possible levels, greatly simplifying the spectra.

Applying the parity operator $\hat{E}^*$ to the rovibrational wave function has the effect

$$\hat{E}^* |l_1, l_2, m_2, K; J, M\rangle = (-1)^J |l_1, l_2, -m_2, -K; J, M\rangle \quad (10)$$

The resulting parity-adapted basis functions may the be written as

$$u_{l_1, l_2, m_2, K}^{J, M, P} = \frac{1}{\sqrt{2(1 + \delta_{m_2, 0} \delta_{K, 0})}} [|l_1, l_2, m_2, K; J, M\rangle$$
$$+ (-1)^{J+P} |l_1, l_2, -m_2, -K; J, M\rangle] \quad (11)$$

where $K > 0$ and $P = 0$ and 1 correspond to even and odd parities, respectively, and if $K = 0$, the constraint $m_2 \geq 0$ holds. The combination $m_2 = K = 0$ and $(-1)^{J+P} = -1$ is not allowed.

The effects of the symmetry operations on the parity-adapted basis function $u_{l_1, l_2, m_2, K}^{J, M, P}$ are summarized below, and further details may be found in refs.[72] and:[54]

$$\hat{E}^* u_{l_1, l_2, m_2, K}^{J, M, P} = (-1)^P u_{l_1, l_2, m_2, K}^{J, M, P}$$
$$(12) u_{l_1, l_2, m_2, K}^{J, M, P} = u_{l_2, l_1, m_1, K}^{J, M, P} \quad (K > 0)$$
$$(12) u_{l_1, l_2, m_2, K}^{J, M, P} = (-1)^{J+P} u_{l_2, l_1, -m_1, 0}^{J, M, P} \quad (K = 0)$$
$$(34) u_{l_1, l_2, m_2, K}^{J, M, P} = (-1)^{l_1 + l_2 + P} u_{l_1, l_2, m_2, K}^{J, M, P} \quad (12)$$

In the parity-adapted angular finite basis representation (FBR), the diagonal kinetic energy matrix elements are

$$\langle u_{l_1, l_2, m_2, K}^{J, M, P} | \hat{T}_{\text{diag}} | u_{l_1, l_2, m_2, K}^{J, M, P} \rangle$$
$$= \frac{1}{2m_{pH_2} r_1^2} l_1(l_1 + 1)$$
$$+ \frac{1}{2m_{pH_2} r_2^2} l_2(l_2 + 1) + B_{CO_2} l_1(l_1 + 1)$$
$$+ B_{CO_2}[J(J+1) + l_1(l_1 + 1) + l_2(l_2 + 1)$$
$$- 2K^2 + 2m_2(K - m_2)] \quad (13)$$

and the three types of off-diagonal matrix elements are

$$\langle u_{l_1, l_2, m_2 + 1, K}^{J, M, P} | \hat{T}_{\text{off}} | u_{l_1, l_2, m_2, K}^{J, M, P} \rangle$$
$$= \sqrt{1 + \delta_{m_2, 0} \delta_{K, 0}} B_{CO_2} \lambda_{l_1, K - m_2}^- \lambda_{l_2, m_2}^+ \quad (14)$$

$$\langle u_{l_1, l_2, m_2, K+1}^{J, M, P} | \hat{T}_{\text{Cor}} | u_{l_1, l_2, m_2, K}^{J, M, P} \rangle$$
$$= -\sqrt{1 + \delta_{m_2, 0} \delta_{K, 0}} B_{CO_2} \lambda_{l_1, K - m_2}^+ \lambda_{J, K}^+ \quad (15)$$

$$\langle u_{l_1, l_2, m_2 + 1, K+1}^{J, M, P} | \hat{T}_{\text{Cor}} | u_{l_1, l_2, m_2, K}^{J, M, P} \rangle$$
$$= -\sqrt{1 + \delta_{m_2, 0} \delta_{K, 0}} B_{CO_2} \lambda_{l_2, m_2}^+ \lambda_{J, K}^+ \quad (16)$$

with two special cases

$$\langle u_{l_1, l_2, -m_2, 1}^{J, M, P} | \hat{T}_{\text{Cor}} | u_{l_1, l_2, m_2, 0}^{J, M, P} \rangle =$$
$$- (-1)^{J+P} B_{CO_2} \lambda_{l_1, K - m_2}^- \lambda_{J, 0}^- \quad (m_2 > 0) \quad (17)$$

$$\langle u_{l_1, l_2, -m_2 + 1, 1}^{J, M, P} | \hat{T}_{\text{Cor}} | u_{l_1, l_2, m_2, 0}^{J, M, P} \rangle$$
$$= - (-1)^{J+P} B_{CO_2} \lambda_{l_2, m_2}^- \lambda_{J, 0}^- \quad (m_2 > 0) \quad (18)$$

where $\lambda_{l,m}^\pm = (l(l+1) - m(m \pm 1))^{1/2}$. While the potential is not diagonal in the angular FBR, its matrix element integrals can be

calculated in a grid representation via a three-dimensional transformation for the θ_1, θ_2, and ϕ angles.[53,73] A Gauss–Legendre quadrature was used for the θ_1 and θ_2 angles, and a Gauss–Chebyshev quadrature of the first kind was used to integrate ϕ for even and odd parity cases. The Lanczos algorithm was then used to calculate the rovibrational energy levels by recursively diagonalizing the discretized Hamiltonian matrix.[74-76] In order to account properly for the bosonic nature of the pH_2 molecule, projection operator techniques were used in combination with the Lanczos iteration method to perform calculations only for states which are symmetric with respect to identical pH_2 exchanges. This corresponds to a version of the symmetry-adapted Lanczos (SAL) algorithm[53,77,78] previously used for atomic trimers containing two or more bosonic helium atoms.[79,80]

D. Relative Infrared Transition Intensities. In terms of the basis functions and the Radau coordinate system, the total rovibrational wave function for the nth energy level for a given set of $\{J,M,P\}$ quantum numbers is

$$\Psi_n^{J,M,P}(r_1, r_2, \theta_1, \theta_2, \phi; \alpha, \beta, \gamma) =$$
$$\sum_{\alpha_1, \alpha_2, l_1, l_2, m_2, K} c_{\alpha_1, \alpha_2, l_1, l_2, m_2, K}^{n, J, M, P} f_{\alpha_1}(r_1) f_{\alpha_2}(r_2) u_{l_1, l_2, m_2, K}^{J, M, P}(\theta_1, \theta_2, \phi; \alpha, \beta, \gamma)$$

(19)

in which $f_{\alpha_j}(r_j)$ is a localized DVR basis function for pH_2 particle j, and the coefficient $c_{\alpha_1, \alpha_2, l_1, l_2, m_2, K}^{n, J, M, P}$ is an eigenvector obtained from the Lanczos diagonalization. A second set of iterations along with the approach of Cullum and Willoughby[76] was used to obtain the eigenvectors.

The transition moment for the complex is chosen to lie along the antisymmetry vibrational coordinate of CO_2. The direction cosine describing the angle between the body-fixed z axis and the space-fixed laboratory Z axis is therefore $\mu_Z = \mu_z \cos(\beta)$, which is proportional to the transition dipole strength and governs the intensity of a transition. The expression for the relative dipole intensities for a transition from a lower state n to an upper state n' (set $\mu_z = 1$) is

$$I_{n, J, M, P; n', J', M', P'} \propto 3 e^{-E_n^{J, M, P}/k_B T}$$
$$\times \sum_{M, M'} |\langle \Psi_n^{J, M, P} | \cos(\beta) | \Psi_{n'}^{J', M', P'} \rangle|^2$$
$$= 3 e^{-E_n^{J, M, P}/k_B T} G(J, J' - J)$$
$$\times | \sum_{\alpha_1, \alpha_2, l_1, l_2, m_2, K} c_{\alpha_1, \alpha_2, l_1, l_2, m_2, K}^{n, J, M, P} c_{\alpha_1, \alpha_2, l_1, l_2, m_2, K}^{n', J', M', P'}$$
$$\times O(J, J' - J, K) \delta_{P+P', 1} \delta_{\alpha_1, \alpha_1'} \delta_{\alpha_2, \alpha_2'} \delta_{l_1, l_1'} \delta_{l_2, l_2'} \delta_{m_2, m_2'} \delta_{K, K'} |^2$$

(20)

in which the functions G and O are[53,81]

$$G(J, -1) = \frac{1}{J}$$

$$G(J, 0) = \frac{2J + 1}{4J(J + 1)}$$

$$G(J, +1) = \frac{1}{(J + 1)}$$

$$O(J, -1, K) = -\sqrt{(J + K)(J - K)}$$

$$O(J, 0, K) = 2K$$

$$O(J, +1, K) = -\sqrt{(J + K + 1)(J - K + 1)}$$

(21)

E. Hydrogen or Helium Density in the Body-Fixed Frame. In order to develop some intuitive feeling regarding the nature of these trimer species, it has been helpful to devise a three-dimensional representation of the solvent hydrogen (or helium) part of the wave function in the body-fixed frame.[57] The three-dimensional density of the jth hydrogen or helium associated with $\Psi_n^{J,M,P}$ is defined as

$$\rho_j^{J, M, P, n}(\mathbf{R}) = \int dr_1\, dr_2\, \sin\theta_1\, d\theta_1\, \sin\theta_2\, d\theta_2\, d\phi$$
$$\times |\Psi_n^{J, M, P}(r_1, r_2, \theta_1, \theta_2, \phi; \alpha, \beta, \gamma)|^2 \delta(\mathbf{R} - \mathbf{R}_j[r_1, r_2, \theta_1, \theta_2, \phi])$$

(22)

in which $\mathbf{R}_j[r_1, r_2, \theta_1, \theta_2, \phi]$ is the vector function that maps the Radau coordinates onto the body fixed Cartesian coordinates ($\mathbf{R}_j = \{x_j, y_j, z_j\}$). The above integral can be evaluated on the same grid as was the potential energy integral. However, because of the discrete nature of the Gaussian quadrature grid used for the integration, the density may not always appear to be smooth. In order to obtain a smooth representation of the density, we use a Gaussian representation of the three-dimensional delta function that appears in eq 22

$$\delta(\mathbf{R} - \mathbf{R}_j[r_1, r_2, \theta_1, \theta_2, \phi])$$
$$\approx \frac{1}{(2\pi)^{3/2} \sigma_x \sigma_y \sigma_z} e^{(x - x_i)^2/2\sigma_x^2} e^{(y - y_i)^2/2\sigma_y^2} e^{(z - z_i)^2/2\sigma_z^2}$$

(23)

This expression reduces to an exact delta function in the limit where $(\sigma_x, \sigma_y, \sigma_z) \to (0,0,0)$. Using such a representation of the delta function amounts to performing a Gaussian binning of the density, and leads to a smooth representation of the density, as will be illustrated below.

III. RESULTS AND DISCUSSION

A. Features of the Five-Dimensional Potential Energy Surface. Figure 3 shows how the reduced-dimension, vibrationally averaged, 5D PES for $CO_2-(pH_2)_2$ depends on φ' and θ'_1, when θ'_2, q_1, q_2 are optimized to minimize the energy for each (φ', θ'_1). The global minima well depth of -265.03 cm^{-1} occurs at the T-shape geometry $\theta'_1 = \theta'_2 = 90.0°$ with $q_1 = q_2 = 3.05$ Å and $\varphi' = 69.2°$ (or by symmetry, $\varphi' = 290.8°$). Between these two identical global minima, there exists a saddle point with energy -242.06 cm^{-1} located at $\theta_1' = \theta_2' = 90.0°$ with $q_1 = q_2 = 3.14$ Å and $\varphi' = 180.0°$, which corresponds to a coplanar geometry with the linear CO_2 molecule and two pH_2 particles lying in the same plane, but with the two pH_2 molecules located on opposite sides of the CO_2 molecule. In addition, as is shown in Figure 3 (and perhaps more clearly Figure 4), four equivalent local minima with energy -202.42 cm^{-1} occur at the coplanar geometry ($\varphi' = 0.0°$) with the two pH_2 monomers located on the same side of CO_2 molecule. In this case, one pH_2 is located very near the equatorial position, with $\theta'_i = 88$ or $92°$, while the other is located well above or below that equatorial plane. Parameters characterizing the various stationary configurations and energies for the $CO_2-(pH_2)_2$ trimer are summarized in Table 1, where they are compared with properties of the corresponding $CO_2-(He)_2$ species.

As is shown in Table 1, the energies at all of the various stationary geometries of global minimum, saddle point, and local minimum for $CO_2-(pH_2)_2$ are more than twice as deep as those

7330

dx.doi.org/10.1021/jp200810f |J. Phys. Chem. A 2011, 115, 7327–7337
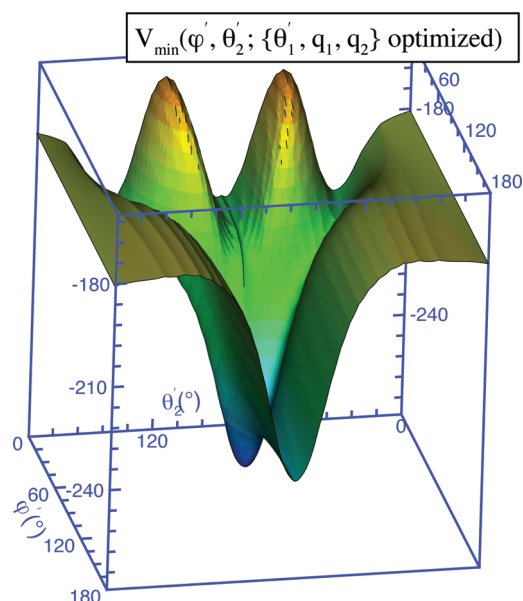
Figure 3. Minimum energy on our vibrationally averaged 5D PES for the $CO_2(v_3 = 0)-(pH_2)_2$ trimer as a function of angle θ'_1 and θ'_2, for optimized values of φ', q_1 and q_2.

Figure 4. Minimum energy (lower panel) and position (upper panel) on our vibrationally averaged 5D PES for $CO_2(v_3 = 0)-(pH_2)_2$ trimer as a function of angle θ'_2, for optimized values of θ'_1, q_1, and q_2, with $\varphi' = 0.0°$.

for $CO_2-(He)_2$. This will be mostly due to stronger polarizability of pH_2 (5.414 au)[82] compared to that of He (1.383 au).[83] Figure 5 shows the minimum energy paths between equivalent global minima as a function of φ', for optimized values of θ'_1, θ'_2, q_1, and q_2, expressed relative to the twice the minimum energy of the corresponding CO_2-pH_2 or CO_2-He dimer. This figure clearly shows that the anisotropy with respect to the dihedral torsional motion of the two pH_2 molecules in $CO_2-(pH_2)_2$ (61.59 cm^{-1}) is almost twice as strong as that for the analogous motion in the $CO_2(v_3 = 0)-(He)_2$ complex (26.01 cm^{-1}). It also shows that the barrier between two adjacent minima of $CO_2-(pH_2)_2$ (23.34 cm^{-1}) is three times higher than that for $CO_2(v_3 = 0)-(He)_2$ (7.51 cm^{-1}). As would be expected, these barrier heights are approximately equal to the well depths for pH_2-pH_2 (24.71 cm^{-1}) and He$-$He (7.65 cm^{-1}) dimers, respectively.

B. Bound State Energies and Infrared Spectrum. Infrared spectra of $CO_2-(p-H_2)_N$ clusters[39] have been observed using a rapid-scan tunable laser spectrometer to probe a pulsed supersonic jet expansion in a manner described previously.[84−86] The expansion gas was a dilute mixture of CO_2 ($\leq 0.1\%$) and pH_2 ($\approx 3\%$) in helium, with the enriched pH_2 prepared in a batch process and mixed with the other gases as described in ref 87. The most complete $CO_2-(pH_2)_2$ data were obtained for the isotope $^{13}C^{16}O_2$ because in this region we had better laser coverage and less interference from atmospheric CO_2. An example of the observed spectra is shown in Figure 6; it was obtained under conditions for which $N = 2$ cluster transitions were reasonably strong, those for $N = 3$ clusters were weaker, and those for $N > 3$ clusters much weaker. The strongest lines were those for $N = 0$ (the CO_2 monomer itself) and $N = 1$ (the CO_2-pH_2 dimer).[85] However, there is also a prominent line at 2283.635 cm^{-1} which can be reliably assigned as the $R(0)$ transition of $CO_2-(pH_2)_2$. Other transitions of the $N = 2$ cluster are significantly weaker, and their detailed assignment only became possible with the help of the present theoretical calculations
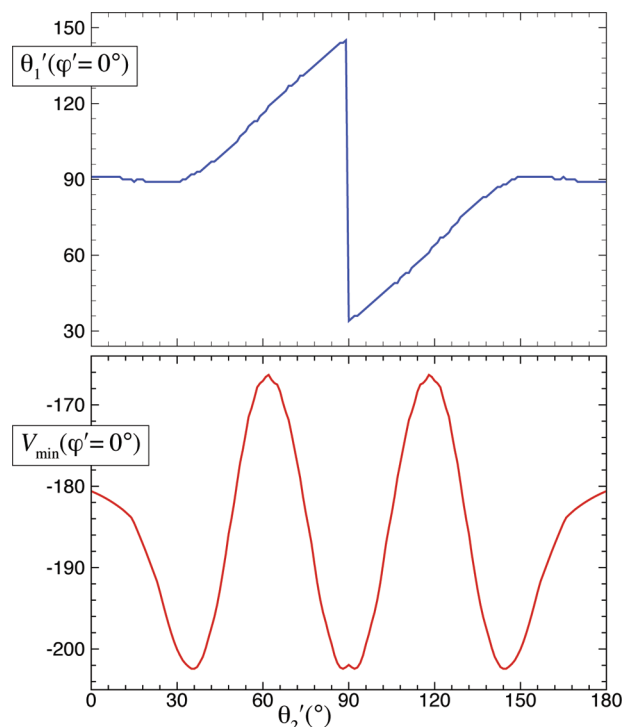
The rovibrational energy levels of the $CO_2-(pH_2)_2$ and $CO_2-(He)_2$ complexes were calculated using the radial DVR and parity-adapted angular FBR method described in section II. The $CO_2-(pH_2)$ and H_2-H_2 potentials were generated by either an "adiabatic-hindered-rotor" or "spherical" average treatment of the H_2 rotation using dimer potentials taken from refs 64 and 68, respectively. For the $CO_2-(He)_2$ complex, the CO_2-He and He$-$He potentials were taken from refs 88 and 89. The inertial rotational constants B_{CO_2} required for these calculations were fixed at the experimental values of 0.390237 and 0.387273 cm^{-1} for $^{13}C^{16}O_2$ and 0.390219 and 0.387141 cm^{-1} for $^{12}C^{16}O_2$ in their ground ($v_3 = 0$) and excited ($v_3 = 1$) states, respectively.[90] The masses were set at 1.00782503207 u for H, 4.00260324 u for ^{4}He, 15.994914635 u for ^{16}O, 12. u for ^{12}C, and 13.003354826 u for ^{13}C. For r_1 and r_2, 40 sine DVR basis functions were used on the domain 3.0−20.0 bohr. For the angular basis, $l_{max} = m_{max} = 25$, and 30 Gauss−Legendre quadrature points were used for each of θ_1 and θ_2, while 64 equally spaced points on the range $[0, 2\pi]$ are used for φ. To accelerate the convergence of the Lanczos calculation, an energy ceiling of 1000 cm^{-1} was imposed.[91] This energy cutoff affects the low-lying levels by less than 0.001 cm^{-1}.

Calculated rovibrational energy levels for $^{13}CO_2(v_3 = 0)-(pH_2)_2$ with $J = 0, 1, 2,$ and 3 are listed in Table 2. Similar tables for complexes formed from the excited ($v_3 = 1$) monomer and for the normal isotopologue $^{12}CO_2-(pH_2)_2$ are provided as online Supporting Information. These energies are expressed relative to the zero-point level, which is bound by 114.050 cm^{-1}. The levels are labeled by quantum numbers $(v_t; J_{K_aK_c})$, where v_t represents the lowest energy van der Waals vibration, which is a torsional motion of the two pH_2 molecules about the CO_2 axis, J is the total angular momentum, and K_a and K_c are the projections of J on the

Table 1. Properties of Stationary Points on the 5D $CO_2-(pH_2)_2$ Potential Energy Surface, and Comparisons with Properies of $CO_2-(He)_2$ surfaces[a]

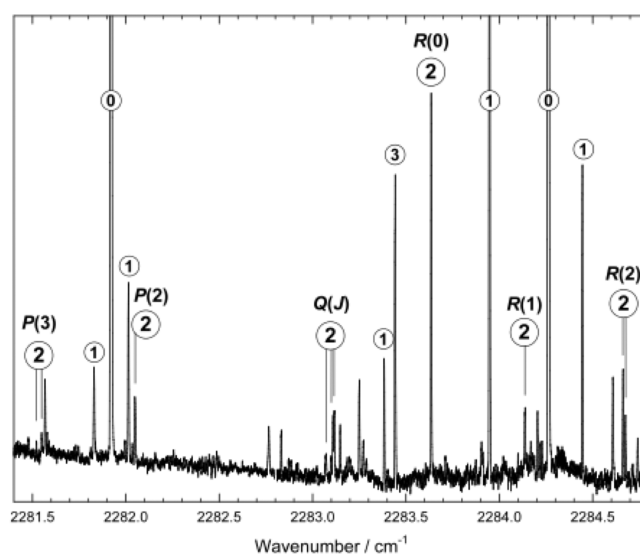|	$CO_2-(pH_2)_2$	$CO_2-(He)_2$
global minimum	{3.05, 3.05, 90.0, 90.0, 69.2, −265.6295}	{2.86, 2.86, 90.0, 90.0, 62.0, −106.59}
	{3.10, 3.10, 90.0, 90.0, 290.8, −264.01}	{2.86, 2.86, 90.0, 90.0, 298.0, −106.59}
saddle point	{3.14, 3.14, 90.0, 90.0, 180.0, −242.0579}	{3.04, 3.04, 90.0, 90.0, 180.0, −99.08}
local minimum	{3.00, 4.00, 36.0, 92.0, 0.0, −202.42}	{2.90, 3.70, 41.0, 93.0, 0.0, −80.58}
	{4.00, 3.00, 88.0, 144.0, 0.0, −202.42}	{3.70, 2.90, 87.0, 139.0, 0.0, −80.58}
	{4.00, 3.00, 92.0, 36.0, 0.0, −202.42}	{3.70, 2.90, 93.0, 41.0, 0.0, −80.58}
	{3.00, 4.00, 144.0, 88.0, 0.0, −202.42}	{2.90, 3.70, 139.0, 87.0, 0.0, −80.58}

[a] All entries are given as: q_1 (Å), q_2 (Å), θ'_1 (deg), θ'_2 (deg), φ' (deg), ΔV (cm^{-1}).
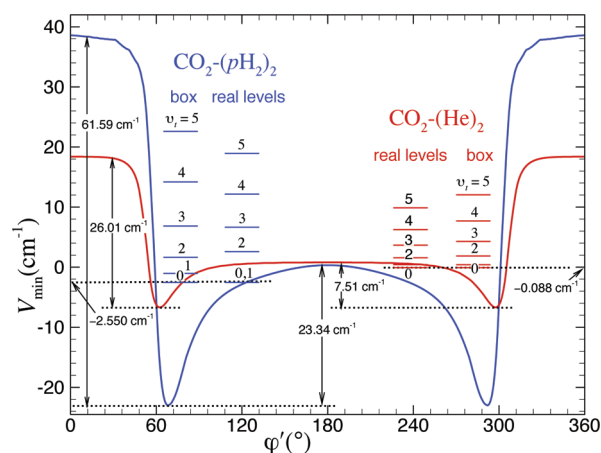
Figure 5. Minimum energy path on our vibrationally averaged 5D PES for a $CO_2(v_3 = 0)-(pH_2)_2$ trimer as a function of torsional angle φ' for optimized values of θ'_1, θ'_2, q_1, and q_2 (blue curve), compared with the analogous minimum energy path for the $CO_2(v_3 = 0)-(He)_2$ trimer (red curve). Energies are expressed relative to twice the minimum energies of the $CO_2(v_3 = 0)-pH_2$ or $CO_2(v_3 = 0)-He$ dimer, respectively.

Figure 6. Observed spectrum of $^{13}C^{16}O_2-(pH_2)_N$ clusters for a jet backing pressure of 10 atm and a jet temperature of −45 °C. The numbers in circles represent the assigned cluster size N ($N = 0$ is the bare CO_2 monomer). Lines belonging to the $N = 2$ cluster of interest here are also labeled $P(J)$, $Q(J)$, or $R(J)$, denoting $\Delta J = -1$, 0, or +1.

a and c inertial axes. For $J = 1$, we assign the K_a and K_c values by sorting the levels in increasing order of energy ($1_{01} < 1_{11} < 1_{10}$). For $J = 2$ and higher, we used the symmetry (parity of the K_a and K_c values) of the $J = 1$ assignment. The $K_a = 2$ levels are therefore inverted from the usual ordering.

As noted above, only levels with A_1^+ and A_1^- symmetry are allowed by nuclear spin statistics for $v_3 = 0$. Since v_3 labels the CO_2 antisymmetric stretch vibration, the allowed rotational symmetries for $v_3 = 1$ are A_2^+ and A_2^-. The strong observed $R(0)$ line of $^{13}CO_2-(pH_2)_2$ corresponds to the transition from the lowest energy A_1^+ level $(0;0_{00})$ in its ground ($v_3 = 0$) state into the A_2^- level $(0;1_{01})$ in its excited ($v_3 = 1$) state. Combining the known $^{13}C^{16}O_2$ monomer v_3 band origin (2283.488 cm^{-1})[90] with our calculated zero-point level energies −114.050 and −114.386 cm^{-1} for $v_3 = 0$ and $v_3 = 1$ complexes yields a calculated value of 2283.676 cm^{-1} for the strong $R(0)$ transition energy, which is just 0.041 cm^{-1} larger than the observed value of 2283.635 cm^{-1}. It turns out that most of this residual difference arises in the calculation of the vibrational shift for $CO_2-(pH_2)_2$ and not in the rotational energies. Hence, in our comparisons of theory with experiment, each transition energy is expressed relative to the corresponding estimate of the $CO_2-(pH_2)_2$ band origin. For absolute comparisons, the resulting differences should

be combined with the 0.041 cm^{-1} discrepancy between the theoretical (2283.152 cm^{-1}) and experimental (2283.111 cm^{-1}) band origins.

These relative infrared transition wavenumbers are listed in Table 3, in order of increasing energy of the lower state level. Calculated values are given for both the hindered-rotor and spherical-average 5D potential energy surfaces. Calculated relative intensities are given for temperatures of 0.7 and 1.5 K, which correspond to the approximate range encountered in the experiment. Subject to the overall selection rules $\Delta J = 0, \pm 1$, and $\Delta P = 1$, there are 19 possible allowed transitions with $J \leq 3$ and $v_t \leq 1$. However, 6 of these have predicted intensities of 1% or less relative to the strong $R(0)$ line, making their observation very unlikely. The remaining 13 predicted transitions are illustrated in Figure 7, where stronger and weaker transitions are distinguished by red and blue labels, respectively. All of these 13 transitions can be assigned to observed infrared lines, as indicated in Table 3, although there are actually just 11 observed lines, because in two cases closely spaced pairs of predicted transitions had been identified as a single observed line. It had been fairly obvious that the stronger observed transitions (bold font in Table 3 and

Table 2. Calculated Rovibrational Levels (in cm^{-1}) with $J = 0$, 1, 2, and 3 for $^{13}C^{16}O_2(v_3 = 0)-(pH_2)_2$, Relative to the Zero-Point Level at -114.050 cm^{-1}[a]

A_1^+	A_2^+	B_1^+	B_2^+	A_1^-	A_2^-	B_1^-	B_2^-
			$J = 0$				
0.000	24.030	28.443	22.375	22.656	31.263	24.826	0.097
$(0;0_{00})$							$(1;0_{00})$
5.130	26.740		30.261			31.490	9.184
$(2;0_{00})$							$(3; 0_{00})$
14.696	30.968		30.916				21.452
$(4;0_{00})$							$(5; 0_{00})$
27.255							30.585
29.969							
			$J = 1$				
	0.743	0.621	0.634	0.725	0.526	0.642	
	$(1;1_{10})$	$(1;1_{01})$	$(0;1_{11})$	$(1;1_{11})$	$(0; 1_{01})$	$(0; 1_{10})$	
	9.765	9.717	5.859	9.857	5.700	5.695	
	$(3; 1_{10})$	$(3; 1_{01})$	$(2;1_{11})$	$(3;1_{11})$	$(2; 1_{01})$	$(2; 1_{10})$	
			$J = 2$				
1.576	1.752	2.121	1.701	1.808	2.025	1.675	1.665
$(0;2_{02})$	$(1;2_{12})$	$(1;2_{21})$	$(0;2_{11})$	$(1;2_{11})$	$(0;2_{21})$	$(0;2_{12})$	$(1;2_{02})$
2.022	11.015	11.161	6.670	10.738	7.147	7.164	2.122
$(0;2_{20})$	$(3;2_{12})$	$(3;2_{21})$	$(2;2_{11})$	$(3;2_{11})$	$(2;2_{21})$	$(2;2_{12})$	$(1;2_{20})$
6.672							10.724
$(2;2_{02})$							$(3;2_{02})$
7.317							11.220
$(2;2_{20})$							$(3;2_{20})$
			$J = 3$				
3.598	3.399	3.222	3.227	3.288	3.141	3.284	3.686
$(0;3_{22})$	$(1;3_{12})$	$(1;3_{03})$	$(0;3_{13})$	$(1;3_{13})$	$(0;3_{03})$	$(0;3_{12})$	$(1;3_{22})$
8.852	4.253	3.691	4.154	4.253	3.586	4.153	12.754
$(2;3_{22})$	$(1;3_{30})$	$(1;3_{21})$	$(0;3_{31})$	$(1;3_{31})$	$(0;3_{21})$	$(0;3_{30})$	$(3;3_{22})$
	12.169	12.166	8.859	12.695	8.054	8.055	
	$(3;3_{12})$	$(3;3_{03})$	$(2;3_{13})$	$(3;3_{13})$	$(2;3_{03})$	$(2;3_{12})$	
	13.258	12.973	9.502	13.287	9.358	9.322	
	$(3;3_{30})$	$(3;3_{21})$	$(2;3_{31})$	$(3;3_{31})$	$(2;3_{21})$	$(2;3_{30})$	

[a] Assignments (in parentheses) are $(v_t; JK_aK_c)$.

red in Figure 7) were really due to $CO_2-(pH_2)_2$ even before the calculations were available, but making assignments for the weaker (blue) ones had to await the present calculations. As shown by the differences (calculated minus observed) in column 4 of Table 3, theory and experiment agree very well: the root-mean-square (rms) deviation is only 0.011 cm^{-1} for the hindered-rotor calculations. The transition energies calculated using the spherical-average surface (column 7) also agree fairly well with experiment, but the associated differences (column 8) are significantly larger, with an rms deviation of 0.021 cm^{-1}.

C. Vibrational Energy Pattern in $CO_2-(pH_2)_2$ vs $CO_2-(He)_2$ Trimers. The $J = 0$ vibrational energies for $^{12}C^{16}O_2-(pH_2)_2$ are listed in Table 4. As is seen there, the binding energy of the ground vibrational level of $^{12}C^{16}O_2(v_3 = 0)-(pH_2)_2$ is 113.9995 cm^{-1}, which is 43.18% of the total three-body well depth of 264.01 cm^{-1}. This well depth is 1.7 cm^{-1} smaller than the sum of twice the 120.50 cm^{-1} well depth[60] of the $^{12}C^{16}O_2-(pH_2)$ dimer plus the 24.71 cm^{-1} depth of the $(pH_2)_2$ potential

from an "adiabatic-hinder-rotor" treatment of pH_2 rotation.[64] However, this ground-state level is bound by 2.20 cm^{-1} *more* than the twice the binding energy of the $^{12}CO_2-(pH_2)$ dimer (54.44 cm^{-1})[60] plus the binding energy of the $(pH_2)_2$ dimer (2.97 cm^{-1}).[64] That additive estimate is of course expected to be approximate, because it neglects the effect of correlation associated with the mixing of the two pH_2 particle wave functions. In contrast, the binding energy of the ground vibrational level of the corresponding $^{12}C^{16}O_2(v_3 = 0)-(He)_2$ trimer is 34.170 cm^{-1}, which is 32.06% of the total three-body well depth of 106.59 cm^{-1} and 11.12% smaller than is the case for the $^{12}C^{16}O_2(v_3 = 0)-(pH_2)_2$ complex. This indicates that two helium atoms have more freedom of movement than do the two pH_2 particles in corresponding complexes formed with CO_2.

The lowest excited vibration of $CO_2-(pH_2)_2$ is associated with the relative "torsional" motion of the two pH_2 molecules on a ring about the CO_2 axis. As is shown in Table 4, for $J = 0$ trimers formed by $CO_2(v_3 = 0)$, excitation energies of 0.098, 5.132, 9.191, 14.709, and 21.471 cm^{-1} are assigned to the $v_t = 1, 2, 3, 4$, and 5 levels of this torsional motion, based on examination of the associated wave functions along the φ' coordinate; see Figure 8. For $^{12}C^{16}O_2-(He)_2$, the corresponding torsional level energies are 0.501, 1.655, 3.752, 6.340, and 9.590 cm^{-1}. The basic nature of these level energy patterns is explained by a simple one-dimensional particle-in-a-box (PIB) model[53]

$$E_n = \frac{\hbar^2 \pi^2}{2\mu L^2}(v_t + 1)^2 \qquad (24)$$

in which μ is the reduced mass of two H_2 or two He moieties, and $L = \Delta\varphi' r_e^{\perp}$ is the length of the box, where $r_e^{\perp}$ is the radial distance of the pH_2 or He from the CO_2 axis and $\Delta\varphi'$ is the angular distance between the walls of the box (see Figure 5). Assuming $L = 12.5664$ Å (using $\Delta\varphi' = 240°$ from Figure 5 with $r_e^{\perp} = 3.0$ Å) for $^{12}C^{16}O_2-(pH_2)_2$ and $L = 13.0900$ Å ($\Delta\varphi' = 250°$ from Figure 5 and $r_e^{\perp} = 3.0$ Å) for the $^{12}C^{16}O_2-(He)_2$ complex, these PIB energies for excited levels of two pH_2 in the $^{12}C^{16}O_2-(pH_2)_2$ complex are 1.045, 4.182, 9.409, 16.727, and 26.136 cm^{-1}, while those for the two He molecules in the $^{12}C^{16}O_2-(He)_2$ complex are 0.485, 1.941, 4.367, 7.763, 12.130 cm^{-1}, respectively. Figure 5 shows that with one exception the overall patterns of level energies calculated from this one-dimension PIB model are in reasonable qualitative agreement with level energies obtained from real five-dimension calculations.
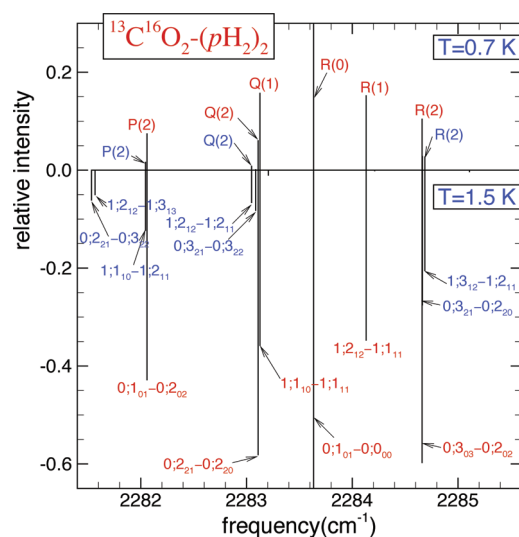
The exception referred to above is the fact that the actual (0.098 cm^{-1}) $v_t = 1 \leftarrow 0$ level spacing for $^{12}C^{16}O_2-(pH_2)_2$ is *very* much smaller than the $v_t = 2 \leftarrow 1$ spacing of 5.034 cm^{-1}. It is also very much smaller than the 0.501 cm^{-1} $v_t = 1 \leftarrow 0$ level spacing in the $^{12}C^{16}O_2-(He)_2$ complex, despite the fact that the latter vibration is associated with a larger reduced mass. In contrast, all other torsional level spacings for $^{12}C^{16}O_2-(pH_2)_2$ are larger than the corresponding values for the $^{12}C^{16}O_2-(He)_2$ complex. However, Figure 5 shows that this small energy spacing of 0.098 cm^{-1} in $^{12}C^{16}O_2-(pH_2)_2$ is readily understood as a tunneling splitting of the ground-state level of the symmetric double minimum potential whose barrier maximum (at $\varphi' = 180°$) corresponds to the two pH_2 molecules lying on opposite sides of the CO_2 axis. The above-barrier closeness of the $v_t = 2$ and 3 levels of this species provides further evidence of this tunneling-pairing behavior. In contrast, for $^{12}C^{16}O_2-(He)_2$ the wells associated with the He−He nearest approach are relatively very much shallower and the $v_t = 0$ level lies only marginally

Table 3. Comparisons of Infrared Transition Energies and Intensities Calculated from the Hindered-Rotor and Spherical-Average 5D Potential Energy Surfaces with Experimental Results for $^{13}C^{16}O_2(\nu_3)-(pH_2)_2$

levels $v_t'; J'_{K_a'K_c'}-v_t''; J''_{K_a''K_c''}$	exptl	hindered-rotor				spherical average	
		calcd	diff	$I_{calcd}(0.7K)$	$I_{calcd}(1.5K)$	calcd	diff
$0{:}1_{01} - 0{:}0_{00}$	**0.524**	**0.524**	**0.000**	**1.000**	**1.000**	0.519	−0.005
$1{:}1_{10} - 1{:}1_{11}$	**0.005**	**0.016**	**0.011**	**0.158**	**0.349**	0.022	0.017
$1{:}2_{12} - 1{:}1_{11}$	**1.026**	**1.020**	**−0.006**	**0.153**	**0.338**	1.006	−0.020
$0{:}1_{01} - 0{:}2_{02}$	**−1.061**	**−1.052**	**0.009**	**0.075**	**0.424**	−1.042	0.019
$0{:}2_{21} - 0{:}2_{02}$		0.446		0.000	0.001	0.414	
$0{:}3_{03} - 0{:}2_{02}$	**1.551**	**1.549**	**−0.002**	**0.105**	**0.590**	1.532	−0.019
$0{:}3_{21} - 0{:}2_{02}$		1.998		0.001	0.004	1.957	
$1{:}1_{10} - 1{:}2_{11}$	−1.061	−1.066	−0.005	0.017	0.121	−1.062	−0.001
$1{:}2_{12} - 1{:}2_{11}$	−0.043	−0.063	−0.020	0.009	0.065	−0.077	−0.034
$1{:}3_{12} - 1{:}2_{11}$	1.564	1.576	0.012	0.028	0.200	1.569	0.005
$1{:}3_{30} - 1{:}2_{11}$		2.439		0.000	0.000	2.353	
$0{:}1_{01} - 0{:}2_{20}$		−1.499		0.000	0.000	−1.458	
$0{:}2_{21} - 0{:}2_{20}$	**−0.003**	**−0.001**	**0.002**	**0.061**	**0.557**	**−0.001**	**0.002**
$0{:}3_{03} - 0{:}2_{20}$		1.102		0.000	0.002	1.117	
$0{:}3_{21} - 0{:}2_{20}$	1.551	1.552	0.001	0.029	0.264	1.542	−0.009
$1{:}2_{12} - 1{:}3_{13}$	−1.563	−1.543	0.020	0.001	0.048	−1.521	0.042
$1{:}3_{12} - 1{:}3_{13}$		0.095		0.000	0.010	0.125	
$0{:}2_{21} - 0{:}3_{22}$	−1.589	−1.577	0.012	0.001	0.059	−1.562	0.027
$0{:}3_{21} - 0{:}3_{22}$	−0.038	−0.024	0.014	0.002	0.078	−0.019	0.019
rmsd			0.011				0.021
band origin shift $\Delta\nu_0$	−0.377		0.041				−0.039

^{a} All energies are in cm^{-1} and diff. ≡ {rmcalc − exptl}, while the most intense transitions are shown in bold font.

Figure 7. Calculated infrared spectra of $CO_2-(pH_2)_2$ trimers for temperatures of 0.7 K (upward pointing lines) and 1.5 K (downward pointing lines), respectively. All intensities are expressed relative to the $0;1_{01}-0;0_{00}$ transition, whose intensity is set to 1.

degrees of freedom except the dihedral angle ϕ'. It is immediately clear that the squares of the $v_t = 0$ and 1 wave functions for $^{12}C^{16}O_2-(pH_2)_2$ shown in the upper panel of Figure 8 will be very similar to one another (see also Figure 10), which is a clear signature of tunneling−splitting behavior. In contrast, the analogous probability densities for the $v_t = 0$ and 1 levels of $^{12}C^{16}O_2-(He)_2$ (lower panel) will be quite different from one another. In closing this discussion we note, however, that although this tunneling/splitting discussion has helped elucidate the nature of this very low energy vibrational mode, the fact that both pH_2 and ^{4}He are bosons means that torsion motion levels with odd quantum numbers v_t are not physically allowed for $J = 0$.

D. The "Solvent" Density Distribution in $CO_2-(pH_2)_2$ vs $CO_2-(He)_2$ Trimers. Figure 9 presents the three-dimensional density for the two pH_2 molecules (upper) or two He atoms (lower) in the body-fixed frame, as calculated for the ground state of $CO_2-(pH_2)_2$ and $CO_2-(He)_2$ using the procedure described in section II.C. Isosurfaces are used to represent the three-dimensional densities, and the z axis is defined to lie on the CO_2 molecular axis. The density distribution of the first pH_2 or He particle is represented as a flat disk in the xz plane, while that of the second is spread out in the xy plane. A prominent feature of these representations is the fact that the two pH_2 molecules or two He molecules appear to have very different density distributions. This is an artifact of the fact that the position of the first pH_2 or helium is used to define the xz plane of the body-fixed frame, and its density is therefore completely localized with respect to the y direction. Indeed, the only reason that its density distribution appears to have nonzero width in the y direction (the thickness

below the corresponding barrier maximum, so the tunneling-pairing effect is almost completely suppressed there.

The partial wave functions for the $v_t = 0$, 1, and 2 levels of these two trimer species are shown in Figure 8. The term partial refers to the fact that the wave functions have been integrated over all
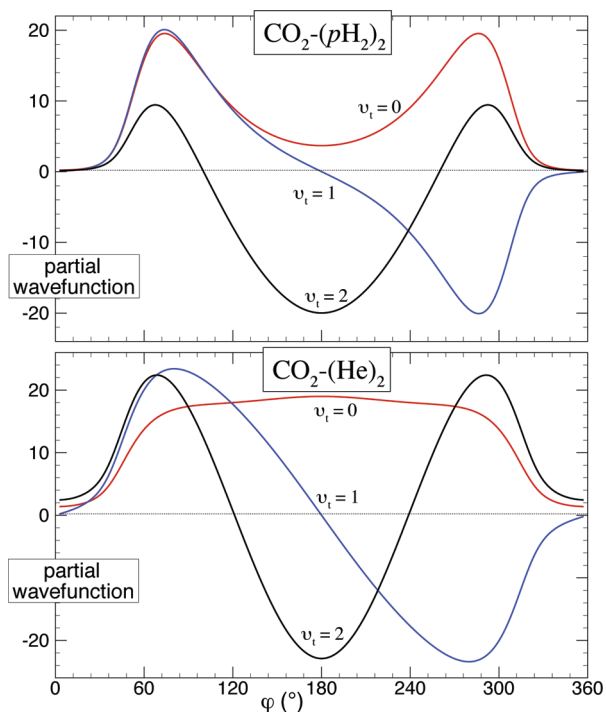
Table 4. Comparisons of Calculated Vibrational Level Energies (in cm^{-1}) for $^{12}C^{16}O_2(\nu_3 = 0)-(pH_2)_2$ with Those for $^{12}C^{16}O_2(\nu_3 = 0)-(He)_2$ Complexes^a

A_1^+	A_2^+	B_1^+	B_2^+	A_1^-	A_2^-	B_1^-	B_2^-
			$^{12}C^{16}O_2-(pH_2)_2$				
0.000 (0)	24.032	28.430	22.364	22.646	31.255	24.829	0.098 (1)
5.132 (2)	26.745	34.860	30.249	33.384	39.992	31.501	9.191 (3)
14.709 (4)	30.960	36.771	30.904	37.140		37.481	21.471 (5)
27.250	36.561		37.412				30.578
29.986	39.050		39.435				37.974
34.125							39.962
36.702							
			$^{12}C^{16}O_2-He_2$				
0.000 (0)	7.729	8.953	7.604	9.209	12.160	9.937	0.501 (1)
1.655 (2)	9.505	11.741	10.373	13.113	15.777	12.992	3.752 (3)
6.340 (4)	12.793	15.113	12.212				9.590 (5)
8.553	13.322		13.950				11.925
11.061							15.437
13.201							
14.933							
15.862							

^{a} Energies are expressed relative to the ground-state level located at —113.9995 cm^{-1} for the former and at −34.1701 cm^{-1} for the latter. All energies smaller than 40.0 cm^{-1} for $^{12}C^{16}O_2-(pH_2)_2$ and smaller than 16.0 cm^{-1} for $^{12}C^{16}O_2-(He)_2$ complexes are listed here. Torsional motion assignments are indicated in parentheses as (ν_t).

Figure 9. Three-dimensional representation of the pH_2 density for the ground-state $CO_2-(pH_2)_2$ trimer (upper panel) in the body-fixed frame, compared with the helium-atom density for a ground-state $CO_2-(He)_2$ trimer (lower panel). The position of the first pH_2 or helium defines the location of the xz plane, while the density of the second pH_2 or He particle is shown in the xy plane. These results were obtained with the values of the Gaussian standard deviations defining the densities set at $\sigma_x = \sigma_z = 0.25$ Å and $\sigma_y = 0.1$ Å for particle-1 and at $\sigma_x = \sigma_y = \sigma_z = 0.25$ Å for particle-2.

Figure 10. The pH_2 density in a $CO_2-(pH_2)_2$ complex as a function of the azimuthal angle φ', compared with with the analogous helium-atom density in a $CO_2-(He)_2$ complex.
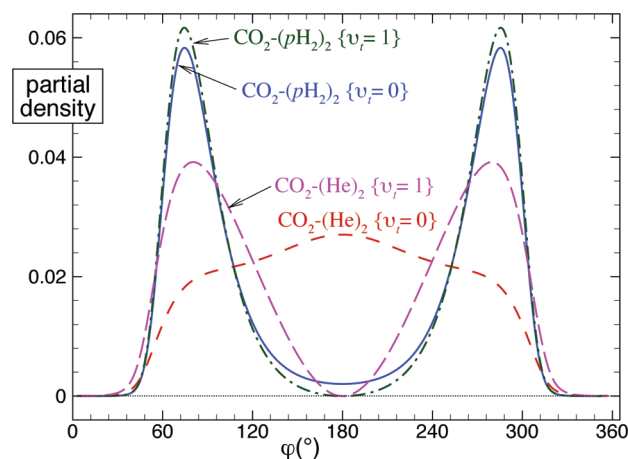

Figure 8. Partial wave functions for the torsional motion (ν_t) of $CO_2-(pH_2)_2$ complexes as a function of the azimuthal angle φ', compared with with those of $CO_2-(He)_2$ complexes.

of reference particle-1) is the use of a finite bin size $(\sigma_y > 0)$ in the calculation. The density distribution of this reference pH_2 or He atom is of course somewhat delocalized in the xz plane, but it is centered at the minimum of the potential energy surface.

As seen in the upper panel of Figure 9, the density distribution of the second pH_2 particle in the $CO_2-(pH_2)_2$ trimer is highly localized, with two density maxima at regions associated with the pH_2-pH_2 potential minimum. In contrast, the density distribution of the second helium atom (lower panel) is highly delocalized relative to the first, being distributed on an
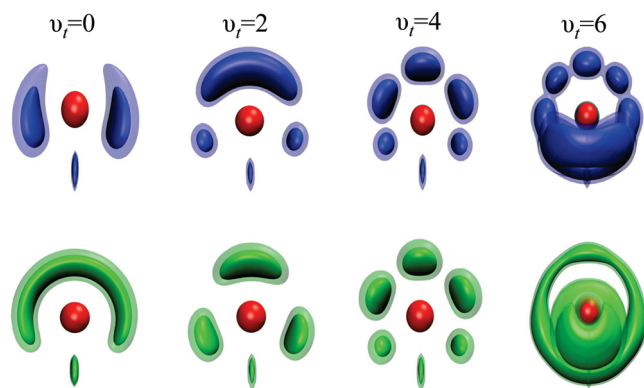
Figure 11. Three-dimensional representations of the "solvent" (pH_2 or He) density for $CO_2-(pH_2)_2$ (upper panels) and $CO_2-(He)_2$ (lower panels) trimers in their four lowest ring-torsion vibrational levels.

incomplete "sausage"-shaped ring wrapped around the CO_2 molecule axis. Moreover, the second He atom appears to have a uniform density over more than half of the range of the azimuthal angle φ', while for the second pH_2 (upper panel of Figure 9), there is a large gap between the two maxima. For both cases, the density for particle-2 is excluded from the region near particle-1 by the short-range repulsive wall of the pH_2-pH_2 or He−He potential.

Figure 10 shows that the reduced density, obtained by integrating the density of the second pH_2 or He moiety with respect to q_1, q_2, θ_1, and θ_2 at each value of φ, has interesting substructure. As shown there, the density distributions are quite different in the $CO_2-(pH_2)_2$ (solid and dash-dot curves) and $CO_2-(He)_2$ (dashed curves) complexes. In particular, the highly localized distribution for pH_2 contrasts sharply with that for He. In addition to the expected excluded volumes near $\varphi' = 0°$ and 360°, for $CO_2-(pH_2)_2$ there are local maxima at $\varphi = 68°$ and 292° corresponding to the pH_2 particles lying at global minimum positions, as shown in Figure 5, with a deep density minimum at $\varphi' = 180°$. In contrast, for $CO_2-(He)_2$ the maximum in the He density is at $\varphi' = 180°$, which corresponds to the two He molecules lying approximately 6.2 Å apart, which is twice the CO_2−He equilibrium distance and also almost double the He−He potential equilibrium distance of $r_e = 2.968$ Å. Of course the distance associated with this density maximum is is much smaller than the 45.6 Å expectation value of the internuclear distance in the ground state of an isolated He_2 molecule, since the relatively strong CO_2−He potential constrains the two He atoms to lie within a ring about the axis of the CO_2. However, the weakness of the He−He potential means that over a φ' range of more than 180°, the two He atoms move almost freely relative to one another.

Finally, Figure 11 shows the "solvent" pH_2 (upper panels) and He (lower panels) densities in the first four allowed torsional levels of $CO_2-(pH_2)_2$ and $CO_2-(He)_2$, respectively. We see there that although the density distribution patterns are very different for $v_t = 0$, they are very similar for the $v_t = 2$ and 4 excited states, both of which correspond to unhindered PIB states. For both systems, the $v_6 = 6$ levels are highest of these PIB-type levels, beyond which this this φ' motion becomes an almost free rotation, and the blurring of the solvent density for both species in $v_t = 6$ signals the upper bound to the region in which this PIB-like behavior is defined (see also Figure 5).

IV. CONCLUDING REMARKS

Calculated rovibrational energy levels and infrared spectra for $^{13}C^{16}O_2-(pH_2)_2$ have been obtained from a global potential energy surface defined as a sum of accurate CO_2-pH_2 and pH_2-pH_2 pair potentials. The predictions are in good agreement with new experimental measurements of these infrared transitions, showing that the spectrum can be reliably predicted by this additive approach. Small remaining differences between experiment and theory may in part be due to our neglect of three-body contributions to the interaction energy. In any case, a reduced-dimension treatment of pH_2 rotation based on a "adiabatic hindered-rotor" average over its relative orientations yields much more accurate predictions than are obtained using the conventional spherical average.

A recently proposed approach[57] for visualizing the para-hydrogen or helium density in the body-fixed frame is used to show the density of the second pH_2 or helium atoms relative to the position of the first. Three-dimensional pictures clearly show that the pH_2 density distribution in the ground vibrational state of $CO_2-(pH_2)_2$ is highly localized, with two maxima, while the He distribution in $CO_2-(He)_2$ is delocalized, with one maximum lying in an incomplete "sausage"-shaped ring about the CO_2 axis. In $CO_2-(pH_2)_2$, the small separation between the two lowest vibrational levels (0.098 cm^{-1}) can be characterized as a ground-state tunneling splitting associated with the relative "torsional" motion of the two pH_2 molecules. In contrast, the larger value (0.501 cm^{-1}) of the analogous separation for $CO_2-(He)_2$ shows that the effective tunneling barrier is much lower in that case.

■ ASSOCIATED CONTENT

S **Supporting Information.** Tables of calculated rovibrational levels. This material is available free of charge via the Internet at http://pubs.acs.org.

■ AUTHOR INFORMATION

Corresponding Author
*E-mail: pnroy@uwaterloo.ca.

■ ACKNOWLEDGMENT

■ REFERENCES

(1) Sindzingre, P.; Ceperley, D. M.; Klein, M. L. *Phys. Rev. Lett.* **1991**, 67, 1871.
(2) Cuervo, J. E.; Roy, P. N. *J. Chem. Phys.* **2006**, 125, 124314.
(3) Mezzacapo, F.; Boninsegni, M. *Phys. Rev. Lett.* **2006**, 97, 045301.
(4) Guardiola, R.; Navarro, J. *Phys. Rev. A* **2006**, 74, 025201.
(5) Khairallah, S. A.; Sevryuk, M. B.; Ceperley, D. M.; Toennies, J. P. *Phys. Rev. Lett.* **2007**, 98, 183401.
(6) Navarro, J.; Guardiola, R. *J. Low Temp. Phys.* **2007**, 148, 857.
(7) Mezzacapo, F.; Boninsegni, M. *Phys. Rev. A* **2007**, 7S, 33201.

7336

dx.doi.org/10.1021/jp200810f |*J. Phys. Chem. A* 2011, 115, 7327–7337

(8) Mezzacapo, F.; Boninsegni, M.; , *Phys. Rev. A* **76**, 021201 (Aug **2007**).

(9) Cuervo, J. E.; Roy, P. N. *J. Chem. Phys.* **2008**, *128*, 224509.

(10) Guardiola, R.; Navarro, J. *Cent. Eur. J. Phys.* **2008**, *6*, 33.

(11) Guardiola, R.; Navarro, J. *J. Chem. Phys.* **2008**, *128*, 144303.

(12) Cuervo, J. E.; Roy, P.-N. *J. Chem. Phys.* **2009**, *131*, 114302.

(13) Warnecke, S.; Sevryuk, M. B.; Ceperley, D. M.; Toennies, J. P.; Guardiola, R.; Navarro, J. *Eur. Phys. J. D* **2010**, *56*, 353.

(14) Sevryuk, M.; Toennies, J.; Ceperley, D. *J. Chem. Phys.* **2010**, *133*, 064505.

(15) Navarro, J.; Guardiola, R. *Int. J. Quantum Chem.* **2011**, *111*, 463.

(16) Grebenev, S.; Toennies, J. P.; Vilesov, A. F. *Science* **1998**, *289*, 2083.

(17) Toennies, J. P.; Vilesov, A. F. *Annu. Rev. Phys. Chem.* **1998**, *49*, 1.

(18) Tang, J.; Xu, Y.; McKellar, A. R. W.; Jäger, W. *Science* **2002**, *297*, 2030.

(19) Tang, J.; McKellar, A. R. W. *J. Chem. Phys.* **2003**, *119*, 754.

(20) Xu, Y.; Jäger, W. *J. Chem. Phys.* **2003**, *119*, 5457.

(21) Tang, J.; McKellar, A. R. W. *J. Chem. Phys.* **2003**, *119*, 5467.

(22) Tang, J.; McKellar, A. R. W.; Mezzacapo, F.; Moroni, S. *Phys. Rev. Lett.* **2004**, *92*, 145503.

(23) Tang, J.; McKellar, A. R. W. *J. Chem. Phys.* **2004**, *121*, 181.

(24) McKellar, A. R. W. *J. Chem. Phys.* **2007**, *127*, 044315.

(25) McKellar, A. R. W.; Xu, Y.; Jäger, W. *J. Phys. Chem. A* **2007**, *111*, 7329.

(26) McKellar, A. R. W. *J. Chem. Phys.* **2008**, *128*, 044308.

(27) Surin, L. A.; Potapov, A. V.; Dumesh, B. S.; Schlemmer, S.; Xu, Y.; Raston, P. L.; Jäger, W. *Phys. Rev. Lett.* **2008**, *101*, 233401.

(28) Grebenev, S.; Lugovoi, E.; Sartakov, B. G.; Toennies, J. P.; Vilesov, A. F. *Faraday Discuss.* **2001**, *118*, 19.

(29) Grebenev, S.; Sartakov, B. G.; Toennies, J. P.; Vilesov, A. F. *J. Chem. Phys.* **2001**, *114*, 617.

(30) Grebenev, S.; Sartakov, B.; Toennies, J. P.; Vilesov, A. *Phys. Rev. Lett.* **2002**, *89*, 225301.

(31) Grebenev, S.; Sartakov, B. G.; Toennies, J. P.; Vilesov, A. F. *J. Chem. Phys.* **2003**, *118*, 8656.

(32) Moore, D. T.; Miller, R. E. *J. Chem. Phys.* **2003**, *119*, 4713.

(33) Moore, D. T.; Miller, R. E. *J. Phys. Chem. A* **2004**, *108*, 1930.

(34) Moroni, S.; Botti, M.; De Palo, S.; McKellar, A. R. W. *J. Chem. Phys.* **2005**, *122*, 094314.

(35) Tang, J.; McKellar, A. R. W. *J. Chem. Phys.* **2004**, *121*, 3087.

(36) Tang, J.; McKellar, A. R. W. *J. Chem. Phys.* **2005**, *123*, 114314.

(37) Grebenev, S.; Sartakov, B. G.; Toennies, J. P.; Vilesov, A. F. *Europhys. Lett.* **2008**, *83*, 66008.

(38) Grebenev, S.; Sartakov, B. G.; Toennies, J. P.; Vilesov, A. F. *J. Chem. Phys.* **2010**, *132*, 064501.

(39) Li, H.; Le Roy, R. J.; Roy, P.-N.; McKellar, A. R. W. *Phys. Rev. Lett.* **2010**, *105*, 133401.

(40) Paolini, S.; Fantoni, S.; Moroni, S.; Baroni, S. *J. Chem. Phys.* **2005**, *123*, 114306.

(41) Li, H.; Blinov, N.; Roy, P.-N.; Le Roy, R. J. *J. Chem. Phys.* **2009**, *130*, 144305.

(42) Paesani, F.; Gianturko, F. A.; Whaley, K. B. *J. Chem. Phys.* **2001**, *115*, 10225.

(43) Paesani, F.; Viel, A.; Gianturco, F. A.; Whaley, K. B. *Phys. Rev. Lett.* **2003**, *90*, 73401.

(44) Paesani, F.; Whaley, K. B. *J. Chem. Phys.* **2004**, *121*, 4180.

(45) Moroni, S.; Sarsa, A.; Fantoni, S.; Schmidt, K. E.; Baroni, S. *Phys. Rev. Lett.* **2003**, *90*, 143401.

(46) Blinov, N.; Song, X.-G.; Roy, P.-N. *J. Chem. Phys.* **2004**, *120*, 5916.

(47) Blinov, N.; Roy, P.-N. *J. Low Temp. Phys.* **2005**, *140*, 235.

(48) Blinov, N.; Roy, P.-N. *Advances in Quantum Monte Carlo*; ACS Symposium Series 953; American Chemical Society: Washington, DC, 2007; p 165.

(49) Paesani, F.; Whaley, K. B. *J. Chem. Phys.* **2006**, *104*, 61.

(50) Moroni, S.; Blinov, N.; Roy, P.-N. *J. Chem. Phys.* **2004**, *121*, 3577.

(51) Xu, Y. J.; Blinov, N.; Jäger, W.; Roy, P. N. *J. Chem. Phys.* **2006**, *124*, 081101.

(52) Topic, W.; Jäger, W.; Blinov, N.; Roy, P. N.; Botti, M.; Moroni, S. *J. Chem. Phys.* **2006**, *125*, 144310.

(53) Wang, X.-G.; Carrington, T., Jr.; Tang, J.; McKellar, A. R. W. *J. Chem. Phys.* **2005**, *123*, 34301.

(54) Tang, J.; McKellar, A. R. W.; Wang, X.-G.; Carrington, T., Jr. *Can. J. Phys.* **2009**, *87*, 417.

(55) Wang, X.-G.; Carrington, T., Jr.; McKellar, A. R. W. *J. Phys. Chem. A* **2009**, *113*, 13331.

(56) Wang, X.-G.; Carrington, T., Jr. *Can. J. Phys.* **2010**, *88*, 779.

(57) Li, H.; Liu, Y. D.; Jäger, W.; Le Roy, R. J.; Roy, P.-N. *Can. J. Chem.* **2010**, *88*, 1146.

(58) Wang, L.; Yang, M. H.; McKellar, A. R. W.; Zhang, D. H. *Phys. Chem. Chem. Phys.* **2007**, *9*, 131.

(59) Ran, H.; Zhou, Y. Z.; Xie, D. Q. *J. Chem. Phys.* **2007**, *126*, 204304.

(60) Li, H.; Roy, P.-N.; Le Roy, R. J. *J. Chem. Phys.* **2010**, *132*, 214309.

(61) Zhou, Y. Z.; Ran, H.; Xie, D. Q. *J. Chem. Phys.* **2006**, *125*, 174310.

(62) Jankowski, P.; Szalewicz, K. *J. Chem. Phys.* **2005**, *123*, 104301.

(63) McKellar, A. R. W. *J. Chem. Phys.* **2005**, *122*, 084320.

(64) Li, H.; Roy, P.-N.; Le Roy, R. J. *J. Chem. Phys.* **2010**, *133*, 104305.

(65) Mladeovic, M. *J. Chem. Phys.* **2000**, *112*, 1070.

(66) Gatti, F.; Lung, C.; Menou, M.; Justum, Y.; Nauts, A.; Chapuisat, X. *J. Chem. Phys.* **1998**, *108*, 8804.

(67) Yu, H.-G. *Chem. Phys. Lett.* **2002**, *365*, 189.

(68) Patkowski, K.; Cencek, W.; Jankowski, P.; Szalewicz, K.; Mehl, J. B.; Garberoglio, G.; Harvey, A. H. *J. Chem. Phys.* **2008**, *129*, 094304.

(69) Light, J. C.; Hamilton, I. P.; Lill, J. V. *J. Chem. Phys.* **1985**, *82*, 1400.

(70) Colbert, D. T.; Miller, W. H. *J. Chem. Phys.* **1992**, *96*, 1982.

(71) Zare, R. N. *Angular Momentum*; Wiley: New York, 1988.

(72) Wang, X.-G.; Carrington, T., Jr. *J. Phys. Chem. A* **2007**, *111*, 10220.

(73) Lin, S. Y.; Guo, H. *J. Chem. Phys.* **2002**, *111*, 5183.

(74) Lanczos, C. *J. Res. Natl. Bur. Stand.* **1950**, *45*, 255.

(75) Golub, G. H.; van Loan, C. F. *Matrix Computations*; Johns Hopkins University Press: Baltimore, MD, 1989.

(76) Cullum, J. K.; Willoughby, R. A. *Lanczos Algorithms for Large Symmetric Eigenvalue Com- putations*; Birkhauser: Boston, MA, 1985.

(77) Wang, X.-G.; Carrington, T., Jr. *J. Chem. Phys.* **2001**, *114*, 1473.

(78) Chen, R.; Guo, H. *J. Chem. Phys.* **2001**, *114*, 1467.

(79) Roy, P.-N. *J. Chem. Phys.* **2003**, *119*, 5437.

(80) Liu, Y. D.; Roy, P.-N. *J. Chem. Phys.* **2004**, *121*, 6282.

(81) McCoy, A. B.; Darr, J. P.; Boucher, D. S.; Winter, P. R.; Bradke, M. D.; Loomis, R. A. *J. Chem. Phys.* **2004**, *120*, 2677.

(82) Bishop, D. M.; Cheung, L. M. *J. Chem. Phys.* **1980**, *72*, 5125.

(83) Parker, G. A.; Snow, R. L.; Pack, R. T. *J. Chem. Phys.* **1976**, *64*, 1668.

(84) Brookes, M. D.; Xia, C.; Tang, J.; Anstey, J. A.; Fulsom, B. G.; Au Yong, K.-X.; King, J. M.; McKellar, A. R. W. *Spectrochim. Acta, Part A* **2004**, *60*, 3235.

(85) McKellar, A. R. W. *J. Chem. Phys.* **2005**, *122*, 174313.

(86) McKellar, A. R. W. *Appl. Phys. B: Lasers Opt.* **2008**, *90*, 213.

(87) Tang, J.; McKellar, A. R. W. *J. Chem. Phys.* **2002**, *116*, 646.

(88) Li, H.; Le Roy, R. J. *Phys. Chem. Chem. Phys.* **2008**, *10*, 4128.

(89) Jeziorska, M.; Cencek, W.; Patkowski, K.; Jeziorski, B.; Szalewicz, K. *J. Chem. Phys.* **2007**, *127*, 124303.

(90) Guelachvili, G. *J. Mol. Spectrosc.* **1980**, *79*, 72.

(91) Bramley, M.; Tromp, J.; Carrington, T., Jr.; Corey, G. *J. Chem. Phys.* **1994**, *100*, 6175.